Petroleum Science 23 (2026) 5853–5869

Contents lists available at ScienceDirect

Petroleum Science

journal homepage: www.keaipublishing.com/en/journals/petroleum-science

Original Paper

Influence of pore structure on high-voltage electrical pulse rock breaking: A coupled numerical approach

Yu-Wei Li [a], Xin-Hui Guo [a], Xue-Wei Liu [b], Yuan Pan [b], Yong-Hui Xiao [c], Hui-Min Tang [d], Dmitriy A. Martyushev [e], Zi-Han Sun [a,*]

[a] School of Environment, Liaoning University, Shenyang, 110036, Liaoning, China
[b] Petroleum Engineering Research Institute, PetroChina DaGang Oilfield Company, Tianjin, 300280, China
[c] School of Physics, Liaoning University, Shenyang, 110036, Liaoning, China
[d] Hainan Branch CNOOC (China) Co., Ltd., Haikou, 570311, Hainan, China
[e] Department of Oil and Gas Technologies, Perm National Research Polytechnic University, Perm, 614990, Russia

A R T I C L E I N F O

Article history:
Received 28 April 2025
Received in revised form
11 February 2026
Accepted 20 May 2026
Available online 27 May 2026

Edited by Xi Zhang

Keywords:
Deep rock breaking
High-voltage electrical pulse
Electrical breakdown path
Pore structure
Fracture mechanism
Stress concentration effect

A B S T R A C T

High-voltage electrical pulse (HVEP) rock-breaking technology is extensively utilized due to its advantages of high energy density, controllable fragmentation zones, and tunable energy output. However, the intricate pore structures within rock masses can significantly affect their electrical and mechanical properties, thereby influencing HVEP performance. To elucidate the mechanisms by which pore structure influences rock-breaking outcomes, this study integrates the finite difference method (FDM) and stochastic propagation model to simulate the electrical breakdown paths. Furthermore, the numerical simulations of HVEP-induced rock fragmentation are conducted using the discrete element method (DEM) based on thermo-mechanical coupling theory. The results demonstrate that the pore structure strongly impacts both the complexity of the breakdown path and the resulting fragmentation efficiency. In non-porous rocks, breakdown paths are primarily governed by rock heterogeneity, resulting in a complex branching structure. In contrast, in porous rocks, breakdown paths are guided by pore spaces, which reduces path complexity. Notably, under constant porosity, pore diameter exerts a nonlinear influence on path complexity. Smaller pore diameters, which correspond to a higher pore density, significantly enhance path complexity. Conversely, as pore diameter increases and the number of pores decreases, path complexity exhibits a 'rebound' as the governing mechanism shifts back to inherent rock heterogeneity. Moreover, the pore structure induces stress concentration, promoting fracture initiation and propagation, which enhances rock-breaking performance. Although rocks with small pores exhibit higher breakdown-path complexity, their fragmentation efficiency is lower than that of large-pore rocks. This finding highlights the dominant role of pore-induced stress field alterations. This study provides valuable theoretical guidance for the application of HVEP rock-breaking technology in porous rock fragmentation.

1. Introduction

As the global economy continues to expand, the consumption of coal, oil, natural gas, and other resources is experiencing rapid growth. Consequently, shallow resources are being depleted, and deep resource extraction is becoming the "new normal" (Cong et al., 2026; Qiao et al., 2013). As the depth of resource extraction increases, the in-situ stress on the rock strata gradually rises, and the strength and elastic modulus of the rock show consistent growth (Li et al., 2024; Xie et al., 2022). These challenging conditions impose significant limitations on traditional rock-breaking technologies, characterized by accelerated tool wear, diminished operational efficiency, and escalating costs (Fu et al., 2022; Hassanpour, 2018; Zhou et al., 2021). Thus, rock-breaking technology has become a bottleneck hindering deep resource extraction. There is an urgent necessity to develop innovative, cost-

* Corresponding author.
E-mail address: sunzihan20180313@126.com (Z.-H. Sun).
Peer review under the responsibility of China University of Petroleum (Beijing).

https://doi.org/10.1016/j.petsci.2026.05.032
1995-8226/

effective, and highly efficient rock-breaking technologies to overcome these barriers.

In recent years, significant advancements in rock-breaking technologies, including water jets, microwaves, and lasers, have provided innovative methodologies for deep rock-breaking applications (Wang et al., 2026; Wei et al., 2026). Water jet technology utilizes high-pressure pumps to accelerate liquid water through specialized nozzles, generating high-velocity jets with substantial kinetic energy. However, as in-situ stress and rock strength increase with depth, its breaking efficiency is significantly reduced. This necessitates a sharp escalation in pump pressure, which imposes more stringent requirements on the sealing integrity and operational safety of the equipment (Liu et al., 2015). Concurrently, microwave and laser-based rock-breaking technologies, which utilize thermal stress mechanisms, have demonstrated notable progress. Microwave-assisted breaking exploits the differential energy absorption of various mineral components, inducing localized thermal stresses that trigger rock failure (Sun et al., 2025). Similarly, laser rock-breaking technology focuses high-energy laser emissions on the rock surface to induce localized melting and vaporization (Yang et al., 2025). Nevertheless, these thermal-effect-based technologies require localized or volumetric treatment, leading to high specific energy consumption that hinders large-scale engineering deployment (Zheng and He, 2021). Given the inherent limitations of these technologies, which are challenging to address in the short term, high-voltage electrical pulse (HVEP) technology has attracted growing research interest (Jin et al., 2026; Liu et al., 2025).

HVEP rock-breaking technology offers distinct advantages, including controllable energy release (Biela et al., 2009), high energy density (Li et al., 2018b; Zhang et al., 2023a), selective fragmentation (Schiegg et al., 2015), and environmental sustainability (Kang et al., 2022). Consequently, it represents a promising solution to the technical bottlenecks in deep-resource extraction. HVEP technology utilizes a high-voltage charging power supply to compress and convert lower power ($\times 10^{-1}$ MW) primary electrical energy into higher power ($\times 10^{3}$ MW) energy for storage, which is subsequently discharged into the rock (Burkin et al., 2009). The resulting intense electric field polarizes the rock, fostering the formation of plasma channels consisting of electrons and ions. Once these channels establish a conductive path between the electrodes, substantial electrical energy is injected. This process enables an accumulation of 10–100 J/cm within a nanosecond-to-microsecond timeframe, with instantaneous temperatures reaching up to 10^4 K (Feng et al., 2024). The rapid elevation in temperature within the plasma channel induces its abrupt expansion, generating intense shock waves that lead to the dynamic fracturing of the rock.

During HVEP-induced rock fragmentation in deep formations, the abundant pore structures within the rock mass play a crucial role in influencing fracture behavior (Fu et al., 2024; Lin et al., 2022). Consequently, elucidating the mechanisms by which porosity affects rock fragmentation efficiency is essential for optimizing HVEP performance in field applications. Previous research on HVEP-induced fracturing of porous rocks has primarily focused on two dimensions. The first aspect involves the modeling of breakdown paths. Researchers have employed fractal theoretical models (Pietronero and Wiesmann, 1984) and electro-thermo-mechanical coupling simulations to predict the influence of pore structures on plasma channel propagation. For instance, Liu et al. (2023b) developed a numerical model integrating electric, current, and breakdown fields with solid mechanics, revealing that plasma channels preferentially propagate toward pores. Similarly, Zhu et al. (2020, 2021, 2024) conducted electrical breakdown experiments and simulations to elucidate the localized breakdown mechanisms, demonstrating that mineral composition and pore distribution significantly affect breakdown paths. The second research direction examines the macroscopic fragmentation characteristics of porous rocks under plasma-induced shock waves. Lisitsyn et al. (1999) found that unsaturated rocks exhibited superior fragmentation performance compared to saturated ones, confirming that gas-filled cavities facilitate electric field intensification and promote breakdown near the electrodes. Zhang et al. (2012) conducted HVEP rock-breaking experiments on five rock types, finding that the average breakdown electric field strength correlates positively with porosity. Liu et al. (2023b) further constructed a random-porosity rock model and simulated the electro-discharge process using a multiphysics coupling framework, finding that increased porosity amplifies local electric field intensity in “electrical damage” regions, thereby enhancing fragmentation. Additionally, Vogler et al. (2020) demonstrated that increased pore fluid salinity enhances pore-scale electrical conductivity, intensifies localized Joule heating and thermal expansion stresses, and consequently reduces the rock breakdown voltage while promoting fracture initiation.

Although several studies have reported that pore structures influence breakdown paths and rock failure, the coupled mechanisms by which these effects jointly govern the overall fragmentation process remain insufficiently investigated. To address this gap, the present study constructs a heterogeneous porous rock model based on Voronoi tessellation and couples the FDM with a stochastic propagation model to simulate the electric field distribution and plasma channel evolution. The effects of pore structure and mineral heterogeneity on plasma propagation are investigated from an electro-physical perspective. Furthermore, a DEM incorporating thermo-mechanical coupling is employed to simulate HVEP-induced rock fracturing, thereby elucidating stress evolution and damage mechanisms in porous rocks. The findings are expected to provide theoretical insights and practical guidance for the field application of HVEP rock-breaking technology.

2. Numerical simulation method of rock breaking by HVEP

Based on the characteristics of the three stages of HVEP-induced rock breaking, a feasible numerical simulation framework is established, as illustrated in Fig. 1. This framework consists of three main stages: model construction, breakdown path simulation, and thermo-mechanical coupling rock-breaking simulation. The process

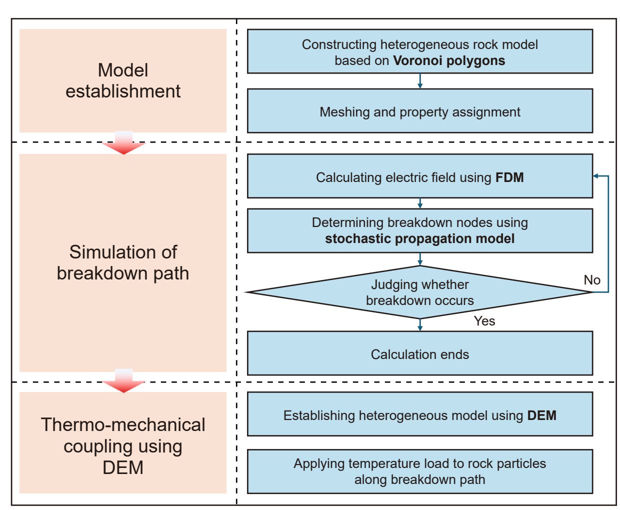

Fig. 1. Numerical simulation framework for rock breaking by HVEP.

begins with the development of a heterogeneous rock model using Voronoi polygons, followed by mesh generation and material property assignment. The breakdown path is then simulated by calculating the electric field using the FDM and identifying breakdown nodes through a stochastic propagation model. Iterative calculations are performed until the breakdown is fully developed. The resulting breakdown path is subsequently superimposed onto the DEM of the rock. Finally, temperature loads are applied to rock particles along the breakdown path to perform thermo-mechanical coupling simulations, enabling analysis of HVEP-induced rock damage.

2.1. Breakdown path propagation simulation

2.1.1. Modeling of rock inhomogeneities

Rocks are composed of crystal grains, including mineral phases, microcrystalline materials, and amorphous phases. Crystals with distinct dielectric properties exhibit different electrical responses during breakdown. Furthermore, the size, morphology, and cementation of crystal particles directly influence the macroscopic mechanical properties. Therefore, the heterogeneous distribution of crystals must be considered when constructing heterogeneous rock models.

The Thiessen polygon (Voronoi tessellation) can produce complex geometrical shapes similar to the microstructure of natural rocks. Therefore, it serves as an effective approach for constructing heterogeneous rock models. The Thiessen polygon is generated by initially assigning seed points and then dividing the spatial region into multiple regions based on these seed points. Any point in each region is closer to its corresponding seed point than to any other seed point. By controlling the distribution and density of seed points, Thiessen polygons can be constructed at different scales. To simulate the naturally random arrangement of mineral grains in rock and avoid the anisotropic bias that may be introduced by manually specifying crystal orientations, this study generates crystal seed points following a uniform Poisson distribution (Abdelaziz et al., 2018; Gulbin and Evangulova, 2003). These Thiessen polygons are assigned to represent mineral crystals such as quartz, feldspar, and mica at a certain scale. The rock model is further subdivided into grid nodes, with each node assigned a corresponding dielectric constant to construct a heterogeneous rock model. In addition, circular pores can be randomly generated based on a specified radius range and porosity. Fig. 2 illustrates a heterogeneous rock model with varying dielectric constants developed by this method.

2.1.2. FDM for solving electric field distribution

The theory of dielectric breakdown in solids posits that, under a strong electric field, rocks undergo continuous polarization, resulting in the formation of breakdown paths. Understanding the evolution of the electric field during breakdown path propagation is essential for elucidating the underlying mechanism. Since the pulse duration (on the order of microseconds) is much longer than the electromagnetic wave propagation time (on the order of nanoseconds), the electrical breakdown process can be regarded as a quasi-static process (Nagel, 2011; Noskov et al., 1995). For HVEP, low-frequency voltages are generally adopted, and the dielectric constant remains constant during the process (Zhao et al., 2024). In addition, electronic and ionic polarization are assumed to respond instantaneously to variations in the electric field. Under these assumptions, the electric field inside the rock is governed by Poisson's equation:

$$\nabla \cdot [\varepsilon(r) \nabla \phi(r)] = -\frac{\rho(r)}{\varepsilon_0} \tag{1}$$

where $\varepsilon(r)$ is the relative permittivity, $\phi(r)$ is the potential field, ε_0 is the vacuum permittivity, and $\rho(r)$ is the space charge density function.

Due to the complex dielectric properties of rocks, the electrical breakdown process is highly nonlinear, rendering the analytical solution of Poisson's equation difficult to obtain. Discretizing Poisson's equation using the FDM and solving it iteratively at each grid node is an effective approach for obtaining a numerical solution (Nagel, 2014). Fig. 3 presents a schematic of the finite difference grid employed to solve Poisson's equation. The finite difference formulation of Poisson's equation is given in Eq. (2).

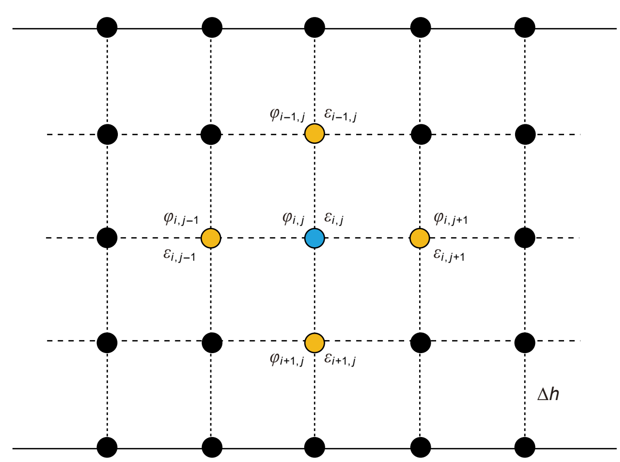

Fig. 3. The finite difference mesh used for solving Poisson's equation.

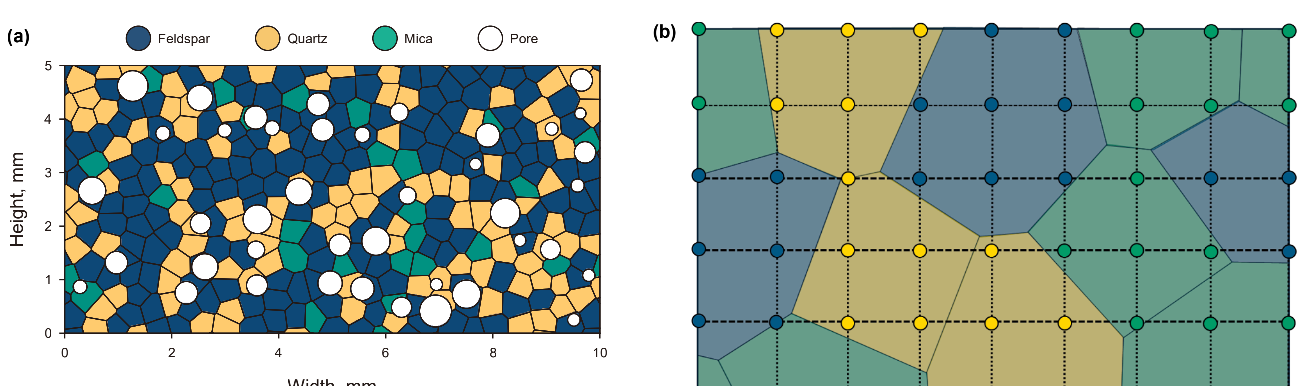

Fig. 2. A heterogeneous model of rock based on Thiessen polygons. (**a**) Mineral crystal and pore distribution, (**b**) grid node.

$$\phi_{i,j} = \frac{\left(\varepsilon_{i,j}\sum_{l,m}\phi_{l,m} + \sum_{l,m}\varepsilon_{l,m}\phi_{l,m} + 2\rho_{i,j}\Delta h^2\right)}{\left(4\varepsilon_{i,j} + \sum_{l,m}\varepsilon_{l,m}\right)} \tag{2}$$

where (l, m) represents the nodes around the current node (i,j), $\phi_{i,j}$ and $\varepsilon_{l,m}$ represents the potentials of the current node and the surrounding nodes, $\varepsilon_{i,j}$ and $\varepsilon_{l,m}$ represents the relative dielectric constants of the current node and the surrounding nodes, $\rho_{i,j}$ represents the bulk charge density of the current node, and Δh represents the distance between the current node and the surrounding nodes.

From Eq. (2), the electric potential at the central node is determined by the potentials and dielectric constants of the four surrounding nodes. The electric potentials at the grid nodes are updated iteratively using Eq. (2) together with the specified boundary conditions. The iteration process terminates when the change in potential between successive updates is less than a predefined tolerance, as specified in Eq. (3). To ensure both accuracy and convergence, the convergence threshold is set to 1% of the minimum grid spacing (0.02 mm), corresponding to 1×10^{-4} kV.

$$e = \left|\min\left(\phi_{i,j} - \phi'_{i,j}\right)\right| < e_r \tag{3}$$

where e is the node potential change before and after update, $\phi_{i,j}$ is the node potential matrix before update, $\phi'_{i,j}$ is the node potential matrix after update, and e_r is the convergence threshold.

2.1.3. *Stochastic propagation models*

The propagation of breakdown paths is governed by the interaction between electrostatic field effects and stochastic effects (Pietronero and Wiesmann, 1984). When simulating the breakdown path, it is essential to account for both effects simultaneously. The following describes the simulation workflow for breakdown path propagation.

2.1.3.1. Rock inhomogeneity modeling. A set of random seed points is initially generated within a rectangular domain. This domain is then partitioned into a fixed number of Thiessen polygons based on these seed points. Each polygon is randomly assigned to mineral phases such as feldspar, quartz, and mica according to a predefined ratio. The region is subsequently meshed, and the dielectric constants corresponding to each mineral phase are assigned accordingly. Additionally, circular voids may be randomly introduced within the domain, with their dielectric constants set to that of air to represent the rock's pore structure.

2.1.3.2. Boundary conditions. The upper boundary of the rock is designated as a positively charged plate with a voltage of ϕ_r kV, while the lower boundary is set as a grounded plate with a voltage of 0 kV. The FDM is applied, iterating multiple times to compute the potential matrix. The method iteratively solves the potential field until convergence is reached. To eliminate lateral edge effects and ensure no lateral electric flux, Neumann boundary conditions are applied to the lateral boundaries, as expressed in Eq. (4). This treatment eliminates the influence of lateral dimensions on the simulation results.

$$\left.\frac{\delta V}{\delta x}\right|_{x=0} = \left.\frac{\delta V}{\delta x}\right|_{x=W} = 0 \tag{4}$$

2.1.3.3. Breakdown node selection. As illustrated in Fig. 4, unbroken nodes adjacent to the breakdown path may become subsequent breakdown nodes and are defined as potential breakdown nodes. The breakdown probability of these nodes is related to the local potential energy. The potential energy of each potential breakdown node is calculated and normalized by the total potential energy of all candidate nodes. The resulting normalized value represents the breakdown probability of each node, as expressed in Eq. (5). A cumulative probability distribution is then constructed from these probabilities, and the next breakdown node is determined by generating a random number between 0 and 1 and identifying the corresponding probability interval.

$$P_{(i,j\to i',j')} = \frac{\left(\frac{1}{2}\varepsilon_{r(i',j')}E^2_{(i',j')}\right)^\eta}{\sum_{(i',j')\in\Gamma}\left(\frac{1}{2}\varepsilon_{r(i',j')}E^2_{(i',j')}\right)^\eta} \tag{5}$$

where (i,j) point indicates the node that has been penetrated, (i',j') points indicate the node to be penetrated, $P_{(i,j\to i',j')}$ indicates the probability of penetration of the node to be penetrated (i',j'), $\varepsilon_{r(i',j')}$ indicates the dielectric constant of the node to be penetrated, $E_{(i',j')}$ indicates the electric field of the node to be penetrated, and Γ indicates the set of nodes to be penetrated.

2.1.3.4. Breakdown path propagation. The propagation of the breakdown path is accompanied by electrical energy release, resulting in a voltage drop. Consequently, after identifying a new breakdown node, its potential is updated according to the modified boundary conditions. The voltage update equation is given in Eq. (6). The FDM is then iteratively applied to update the potential distribution and determine the subsequent breakdown node. This process continues until the breakdown path reaches the boundary.

$$\phi_n = \phi_b - E_d\Delta h \tag{6}$$

where ϕ_n is the new breakdown node potential, kV; ϕ_b is the potential of the previous breakdown node, kV; E_d is the reduction in electric field strength, kV/mm.

2.2. *Electric pulse rock breaking thermo-mechanical coupling model*

A thermo-mechanically coupled numerical simulation based on the DEM was employed to investigate thermal

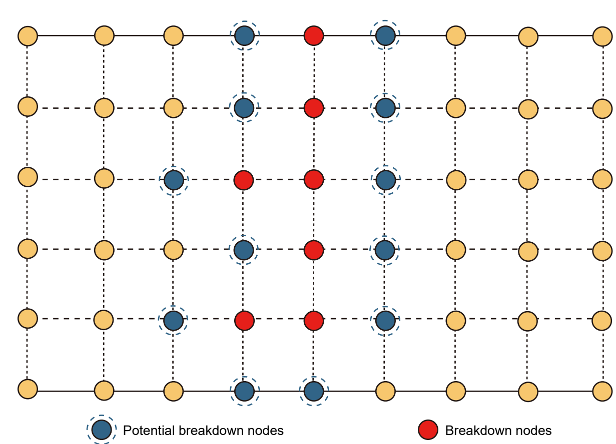

Fig. 4. Breakdown nodes and potential breakdown nodes.

expansion–induced fracturing along the breakdown paths. Within the DEM framework, the rock is discretized into an assembly of microparticles, with particle interactions governed by contact constitutive laws. The parallel bond model (PBM) introduces bonding elements at particle contacts, enabling the transmission of normal and shear forces as well as bending and torsional moments across bonded interfaces (Potyondy and Cundall, 2004). This model has been widely applied in simulations of rock behavior under static and dynamic loading conditions (Li et al., 2018b; Zhang et al., 2023b). In this study, the PBM was adopted to construct the rock model. Bond breakage occurs when the maximum normal or shear stress at particle contacts exceeds the corresponding bond strength, thereby initiating microcrack formation and subsequent propagation. The quantitative evaluation of these maximum stresses is given in Eqs. (7) and (8).

$$\sigma_{\max} = \frac{T}{A} + \frac{|M|}{I}\overline{R} \tag{7}$$

$$\tau_{\max} = \frac{T}{A} + \frac{|M_t|}{J}\overline{R} \tag{8}$$

HVEP rock breaking involves thermo-mechanical coupling, where a high-energy-density current flowing through the plasma channel rapidly heats the breakdown path, leading to thermal expansion of rock particles. The thermo-mechanical model accounts for temperature-dependent variations in particle radius and normal contact force, as defined in Eqs. (9) and (10). Notably, the effect of shock waves generated by the rapid expansion of the plasma channel is significantly greater than that of thermal conduction within the rock (Kang et al., 2022; Liu et al., 2024; Zhao et al., 2025). Therefore, the thermo-mechanical coupling model in this study is primarily used to simulate the process of shock wave generation resulting from the plasma channel expansion.

$$\Delta R = \alpha R \Delta T \tag{9}$$

$$\Delta F_n = -\overline{k_n} A(\overline{\alpha}\overline{L}\Delta T) \tag{10}$$

where ΔR is the change in particle radius; α is the coefficient of thermal expansion; R is the particle radius; ΔT is the change in temperature; ΔF_n is the change in particle normal contact force; $\overline{k_n}$ is the contact surface normal stiffness; A is the contact area; $\overline{\alpha}$ is the contact coefficient of thermal expansion; and $\overline{L}$ is the contact length.

The heterogeneous rock model is constructed using the DEM, as illustrated in Fig. 5. Initially, rock particles are generated within a predefined domain. Subsequently, the pre-established heterogeneous rock model is superimposed onto these particles, which are then classified according to their respective mineral compositions. Appropriate contact parameters are then assigned to both intracrystalline and inter-crystalline contacts. Finally, a temperature load is applied along the breakdown path to simulate the thermo-mechanical coupling effect during HVEP rock breaking.

2.3. Setting of rock electrical property parameters and fine mechanical parameters

To optimize computational efficiency and enhance processing speed, the FDM model for electrical breakdown path calculation was defined with a domain size of 10 mm × 5 mm with a grid resolution of 0.02 mm, resulting in a total of 125,000 grid points. The relative permittivity of quartz, feldspar, mica, and pores was set to 6.0, 12.0, 10.0, and 1.0, respectively (Liu et al., 2023c).

The fine-scale mechanical parameters governing particle interactions are critical for determining the macroscopic mechanical behavior and damage characteristics of the rock. These parameters must be calibrated before performing numerical simulations of HVEP rock breaking. However, the quantitative relationship between fine-scale parameters and macroscopic rock properties remains unclear. Consequently, a trial-and-error approach is commonly adopted for parameter calibration, using the macroscopic mechanical properties of rock specimens as reference benchmarks (Ji and Karlovšek, 2022). The calibration model size was set to 25 mm × 50 mm, consisting of 28,016 particles. The calibration process was guided by the mechanical strength hierarchy of the primary mineral constituents of granite (quartz > feldspar > mica).

Fig. 6(a) compares the uniaxial compressive stress–strain curves obtained from laboratory tests and three numerical simulations. Fig. 6(b) presents the associated damage patterns. Both experimental and numerical specimens exhibit shear failure surfaces, with localized disintegration observed at the specimen tops. Under identical mesoscopic parameters but varying random grain distributions, the simulated peak compressive strengths were 157.6 MPa, 158.7 MPa, and 160.1 MPa, while the elastic moduli were 20.58 GPa, 20.86 GPa, and 20.30 GPa. These values are in good agreement with the experimental peak compressive strength of 159.6 MPa and elastic modulus of 20.82 GPa. These results indicate that the GBM approach produces reproducible macroscopic mechanical responses and that the randomly generated microstructures are representative of real rock behavior.

The calibrated fine-scale parameters were then applied in subsequent simulations, and their values are summarized in Table 1. Notably, at the onset of uniaxial compression, the simulated particles possess stable, pre-established contacts and bonds (Zhang et al., 2022). This configuration omits the initial nonlinear compaction stage, resulting in a linear elastic response at the early stage of loading. This is permissible in PFC simulations (Quan et al., 2023).

To investigate the influence of pore structure on HVEP rock breaking, microscopic pores are introduced by deleting particles. Although the mechanical properties of the rock matrix particles are preserved, this process inevitably reduces the bulk mechanical strength of the specimen. Despite this inherent effect, the research findings provide meaningful insights into the behavior of porous rocks.

Beyond mechanical parameters, fine-scale thermodynamic parameters must also be defined. According to previous studies (Ahrens, 1995; Yang et al., 2018), the thermal expansion coefficients of feldspar, quartz, and mica were set to 8.7×10^{-6}, 24.3×10^{-6}, and 3.0×10^{-6} °C^{-1}, respectively. The specific heat capacities were assigned as 892 J/(kg·K), 710 J/(kg·K), and 760 J/(kg·K), respectively.

2.4. Experimental verification of HVEP rock breaking

2.4.1. Mesh independence verification

To assess the sensitivity of the electric field solution to spatial discretization, a systematic mesh-independence analysis was conducted. Six mesh configurations were examined, ranging from a coarse grid of 100 × 50 to a fine grid of 600 × 300, corresponding to 5,000 to 180,000 total grid points. For each configuration, the electric field was solved under identical boundary conditions, material parameters, and iterative tolerance criteria.

Table 2 summarizes the variations in key physical quantities under different mesh resolutions. When the mesh is refined to 500 × 250, the relative deviation in average electric field intensity is 0.07%, and the relative deviation in total electrostatic energy is

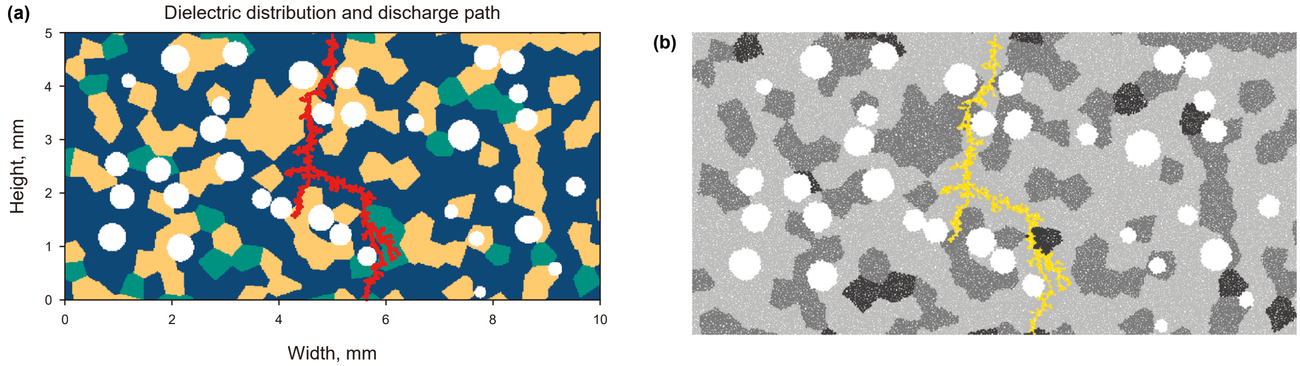

Fig. 5. Heterogeneous rock model. (**a**) Rock breakdown path, (**b**) DEM of heterogeneous rock.

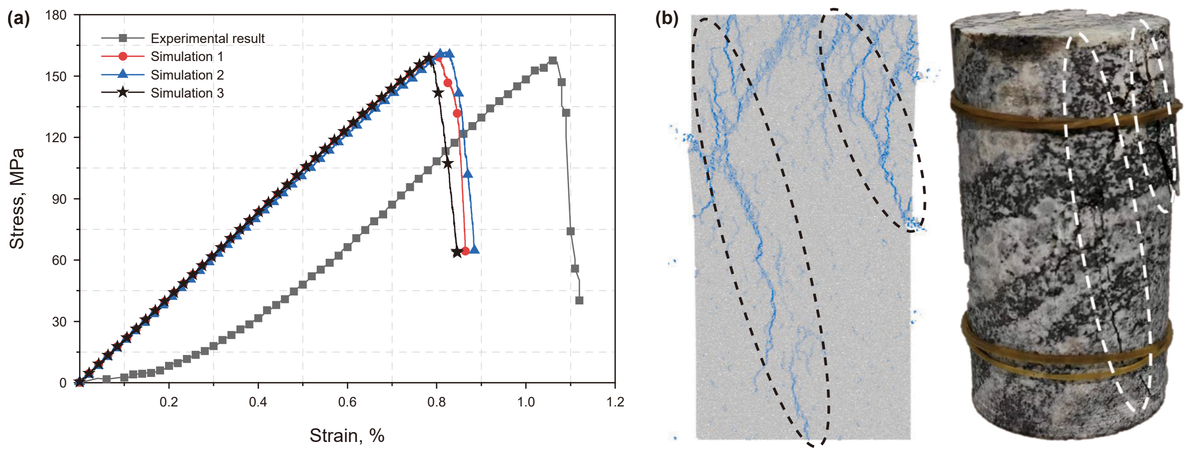

Fig. 6. Calibration results of experimental and numerical simulations. (**a**) Stress-strain curves from experimental and numerical simulations, (**b**) damage patterns from experimental and numerical simulations.

Table 1
Calibrated fine mechanical parameters of rock mineral crystals and crystal boundaries.

Parameter type	Micro-properties of the minerals	Feldspar	Quartz	Mica	Grain boundaries
Electrical parameters	Permittivity	12.0	6.00	10.0	
Mechanical parameters	Minimum particle radius, mm	0.016	0.016	0.016	
	Ratio of maximum to minimum particle radius	1.66	1.66	1.66	
	Porosity	0.08	0.08	0.08	
	Parallel bond modulus, GPa	14.18	15.70	11.72	2.00
	Parallel bond normal to shear stiffness ratio	1.15	1.32	1.50	2.90
	Parallel bond tensile strength, MPa	77.44	97.28	64.00	27.00
	Parallel bond cohesion, MPa	116.10	145.92	96.00	40.50
	Parallel bond friction angle, °	14.00	12.00	16.00	5.00
Thermodynamic parameters	Coefficient of thermal expansion, $^\circ C^{-1}$	8.7×10^{-6}	24.3×10^{-6}	3.0×10^{-6}	
	Specific heat, J/(kg·K)	892	710	760	

Table 2
The performance of key physical quantities under different mesh resolutions.

Mesh size	Number of mesh elements	Average step length, mm	Average electric field, kV/mm	Relative error, %	Total energy	Relative error, %
100×50	5,000	0.1000	9.847	-	88,423	-
200×100	20,000	0.0500	9.914	0.68	89,619	1.34
300×150	45,000	0.0333	9.937	0.23	89,988	0.41
400×200	80,000	0.0250	9.950	0.13	90,213	0.25
500×250	125,000	0.0200	9.957	0.07	90,234	0.02
600×300	180,000	0.0167	9.962	0.05	90,250	0.017

0.02%. Both values are significantly below the commonly accepted numerical tolerance threshold of 2%. Further refinement to 600 × 300 yields negligible improvement while substantially increasing computational cost. Considering the trade-off between solution accuracy and computational efficiency, the 500 × 250 mesh was selected as the optimal mesh resolution for the present study.

2.4.2. Experimental and numerical simulation verification

Huang and Shi (2019) conducted HVEP rock-breaking experiments using cylindrical cement-based grout specimens with a height of 20 mm and a diameter of 20 mm under a voltage of 180 kV at room temperature without external loading. The experimental results are shown in Fig. 7(a). The image of the rock fragments after HVEP is binarized, where the black regions represent breakdown paths formed under high-temperature conditions. To evaluate the accuracy of the proposed numerical model for HVEP rock breaking, a simulation was performed using the described method, and the results are shown in Fig. 7(b). Both the experimental and numerical results indicate that the breakdown path propagates from the upper to the lower rock surface, with branching occurring along the path. The numerical simulation results are in good agreement with the experimental observations, thereby validating the accuracy and reliability of the proposed model.

3. Numerical simulation scheme and results

3.1. Numerical simulation scheme

The rocks in the formation exhibit abundant pore structures. On the one hand, the gas within the pores has significantly different dielectric properties from the surrounding rock, which affects the propagation behavior of the breakdown path. The breakdown path serves as a channel for energy transmission, and the shock wave generated by its expansion can influence the rock damage process. On the other hand, pore structures alter the mechanical properties of the rock, resulting in a breakage behavior that differs significantly from that of dense rock.

Therefore, to elucidate the influence of pore structure on HVEP rock breaking, numerical simulations were performed on porous rocks. A control group without pores was included to represent dense rocks under HVEP, as shown in Table 3. Additionally, numerical simulations were conducted on rocks with identical porosity but varying pore diameters to investigate the effect of pore size on HVEP rock breaking, as shown in Table 4. Since the porosity and pore size of deep rocks vary substantially with lithology, common sedimentary and volcanic rocks typically exhibit porosities of 0.02–0.28 and pore diameters ranging from micrometer to millimeter scales (Bloch et al., 2002; Surma and Geraud, 2003). Based on these findings (Liu et al., 2023b), a representative porosity of 0.1 and a pore diameter range of 0.2–0.7 mm are adopted in this study.

The breakdown path is governed by the competition between deterministic electrostatic field effects and stochastic perturbations (Pietronero and Wiesmann, 1984). This stochasticity arises from electric field fluctuations near the front of the breakdown path. To mitigate stochastic effects, the Monte Carlo method was used to perform multiple simulations. The fractal dimension (D) was quantified using the box-counting method, in which square grids of size (r) are superimposed on the breakdown path, and the number of occupied boxes (N) is counted. The fractal dimension is then calculated as:

$$N(r) \sim r^{-D} \tag{11}$$

Fig. 8 illustrates the evolution of the running mean and 95% confidence interval (CI) of the fractal dimension for both porous and non-porous conditions. The results indicate that the mean stabilizes and the CI width approaches an asymptotic value after approximately 200 repetitions, confirming statistical convergence. To enhance statistical robustness and reduce bias arising from stochasticity, the number of repetitions for each simulation condition was therefore set to 200. Although the resulting 95% CI remains relatively large due to the random distribution of mineral crystals and pores, as well as the intrinsic stochasticity of breakdown propagation, this behavior is physically reasonable.

3.2. Effect of pore structure on electrical breakdown paths

3.2.1. Mechanism of pore structure on breakdown paths

The electric field strength is a critical determinant of breakdown path propagation. Fig. 9 illustrates the breakdown paths and the initial electric field distributions for both porous and non-porous rocks. Fig. 9(a) and (b) show that the breakdown paths exhibit intricate branching structures, with the paths preferentially advancing toward regions of low dielectric constant crystals or pore boundaries.

This phenomenon can be attributed to Maxwell–Wagner interfacial polarization and local field enhancement at dielectric discontinuities. As illustrated in the charge density cloud maps (Fig. 9(c) and (d)), the strong externally applied electric field induces significant electric dipole polarization in both the rock minerals and the pore air, forming bound charge accumulation zones at their interfaces (Joll et al., 2024). In regions with high dielectric permittivity, the polarization-induced bound charges

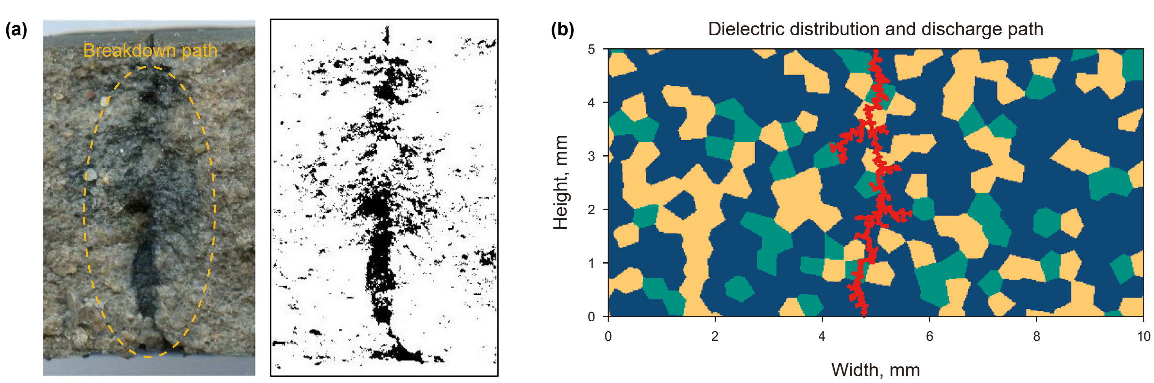

Fig. 7. HVEP rock-breaking effect comparison between experiment and simulation. (**a**) Experimental results of HVEP (Huang and Shi, 2019), (**b**) simulation results of breakdown path.

Table 3
Numerical simulation scheme for the effect of pore on HVEP rock breaking.

Serial number	Voltage, kV	Pore condition	Pore diameter, mm	Repetition frequency
1	100	Without pores	None	200
2	100	Containing pores	0.2–0.6	200

Table 4
Numerical simulation scheme for the effect of pore diameter on HVEP rock breaking.

Serial number	Voltage, kV	Pore area ratio	Pore diameter, mm	Repetition frequency
1	100	0.1	0.2–0.3	200
2	100	0.1	0.3–0.4	200
3	100	0.1	0.4–0.5	200
4	100	0.1	0.5–0.6	200
5	100	0.1	0.6–0.7	200

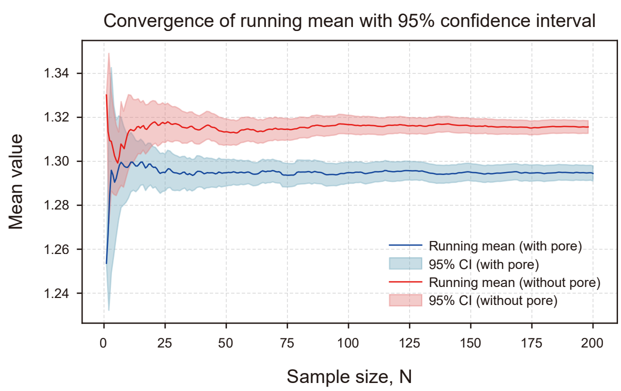

Fig. 8. Variation law of running mean of fractal dimension of breakdown paths.

partially neutralize the internal electric field, yielding a shielding effect. In contrast, regions with low dielectric permittivity exhibit weaker polarization, resulting in local electric field enhancement. Therefore, strong electric field gradients develop at boundaries between regions with contrasting dielectric properties, leading to pronounced field distortion (Fig. 9(e) and (f)). Since regions with intensified electric fields possess higher electrical energy, electrical breakdown preferentially occurs along crystal boundaries and pore boundaries, ultimately forming a complex branching morphology.

Although the breakdown paths in porous and non-porous rocks share similar characteristics, they also exhibit distinct differences. As shown in Fig. 9, the breakdown paths in porous rocks exhibit fewer branches than those in non-porous rocks. Fig. 10 illustrates the average fractal dimensions derived from 200 numerical simulations. The fractal dimension of the breakdown paths is 1.194 in porous rocks and 1.206 in non-porous rocks, suggesting that the presence of pores reduces breakdown-path complexity. The electric field strength primarily governs breakdown path propagation. Consequently, key parameters—including the maximum value (E_{max}), mean electric field strength (E_{avg}), standard deviation (E_{sd}), and coefficient of variation (E_{cv})—were computed, and the results are presented in Table 5. E_{max} and E_{avg} characterize the electric field strength, whereas E_{sd} and E_{cv} quantify its variability. E_{cv} represents a relative measure of variability, defined as the ratio of the standard deviation to the mean electric field strength. These parameters reflect the overall characteristics of the electric field and elucidate the influence of pores on breakdown path dynamics.

As shown in Table 5, the E_{max} of the porous rocks is 198.92 kV/mm, approximately 2.48 times that of non-porous rocks. Similarly, the E_{avg} of porous rocks is higher than that of non-porous rocks. Furthermore, the E_{cv} of porous rocks is 0.519, exceeding that of non-porous rocks. In conjunction with the initial electric field distribution (Fig. 9), these results indicate that pores cause a significant accumulation of interface charges at their boundaries, leading to electric field distortion. This distortion significantly enhances the intensity and spatial variation of the electric field inside the rock. However, the presence of pores reduces the complexity of the breakdown path.

3.2.2. *Influence of pore diameter on breakdown path*

Fig. 11 shows the effect of different pore diameters on breakdown paths. As the pore diameter decreases, the pore density within the rock increases. This variation significantly influences the electric field distribution and the morphology of the breakdown paths.

Fig. 12 illustrates the variation in the mean fractal dimension of breakdown paths across different pore diameter ranges. Results from 200 simulations indicate that the fractal dimension decreases initially and then increases as the pore diameter increases. Specifically, when the pore diameter is 0.2–0.3 mm, the average fractal dimension is 1.1992. As the pore diameter increases to 0.5–0.6 mm, the fractal dimension decreases to 1.1895. However, further increasing the pore diameter to 0.6–0.7 mm leads to an increase in the fractal dimension to 1.1950. These findings suggest that pore diameter influences the complexity of breakdown paths under constant porosity conditions.

Fig. 13(a) and (b) show the influence of pore diameter on the electric field strength within the rock. As the pore diameter decreases from 0.6–0.7 mm to 0.2–0.3 mm, the E_{max} increases from 161.70 kV/mm to 245.73 kV/mm, and the E_{avg} rises from 20.87 kV/mm to 20.95 kV/mm. These results indicate a negative correlation between pore diameter and both E_{max} and E_{avg}. Fig. 13(c) and (d) show the variation of E_{sd} and E_{cv} with pore diameter. When the pore diameter is 0.2–0.3 mm, E_{cv} is 0.536. As the pore diameter increases to 0.6–0.7 mm, E_{cv} decreases to 0.5054. As the pore diameter increases, the fractal dimension of the breakdown path exhibits a trend of initially decreasing and then increasing, whereas the electric field strength and its dispersion decrease monotonically. This asynchronous trend between the fractal dimension and the electric field characteristics (i.e., strength and dispersion) suggests that a threshold may exist during the increase in pore diameter. When this threshold is exceeded, the dominant mechanism influencing the breakdown path propagation undergoes a transition. Specifically, below this threshold, an increase in pore diameter reduces the electric field strength and dispersion, leading to a simplification of the breakdown path and a

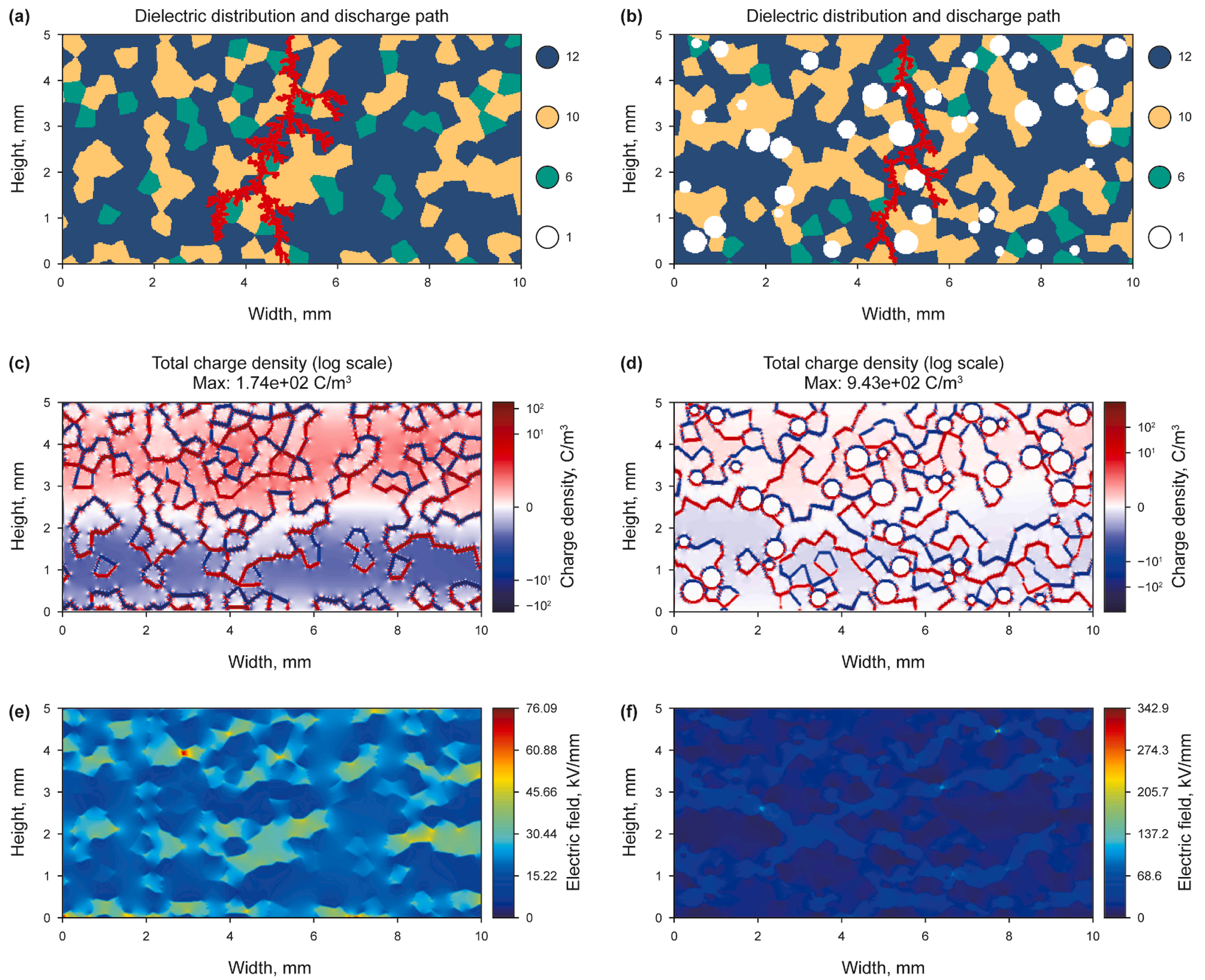

Fig. 9. Breakdown paths, initial charge density distribution, and electric field distribution. (**a**) Breakdown paths in non-porous rocks, (**b**) breakdown paths in porous rocks, (**c**) charge density in non-porous rocks, (**d**) charge density in porous rocks, (**e**) initial electric field strength distribution in non-porous rocks, (**f**) initial electric field strength distribution in porous rocks.

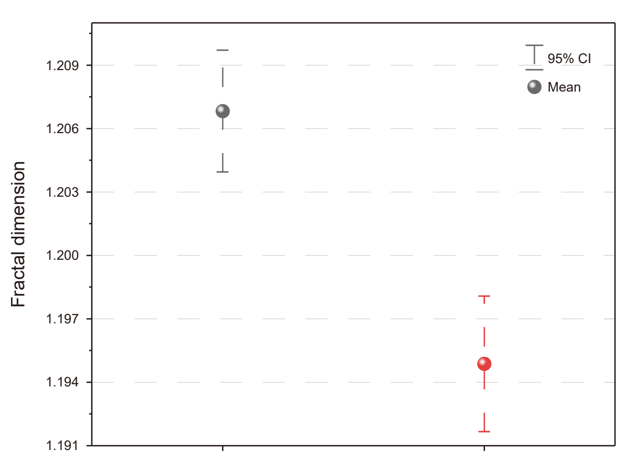

Fig. 10. Fractal dimensions of breakdown paths in porous and non-porous rocks.

subsequent decrease in its fractal dimension. However, once the pore diameter increases beyond this threshold, the electric field dispersion is further weakened. At this point, the guiding effect of pores themselves on the breakdown path may no longer be the dominant factor.

Overall, variations in pore diameter and number significantly influence the morphology of breakdown paths and the electric field distribution within the rock. Rocks with smaller pore diameters exhibit greater electric field dispersion and more complex breakdown paths. As the pore diameter increases, these characteristics undergo stage-wise changes.

3.3. Effect of pore structure on rock fragmentation

3.3.1. Mechanism of pore structure on rock fragmentation

Fig. 14 shows the rock-breaking process of non-porous rock under HVEP. The formation of a breakdown path establishes an electrical circuit between the electrodes, through which a substantial amount of electrical energy is delivered into the rock interior. This leads to a significant temperature rise in particles along the breakdown path. A temperature load of 8,000 K is applied to the particles within this path. At a loading time of 1 μs, numerous cracks initiate and propagate along the breakdown path, indicating the formation of a stress concentration zone. This phenomenon is attributed to the temperature gradient between

Table 5
Parameters of electric field strength inside porous and non-porous rocks.

Electric field strength parameters	E_{max}, kV/mm	E_{avg}, kV/mm	E_{sd}, kV/mm	E_{cv}
Porous rock	198.92	20.91	10.86	0.519
Non-porous rock	79.89	20.47	7.50	0.366

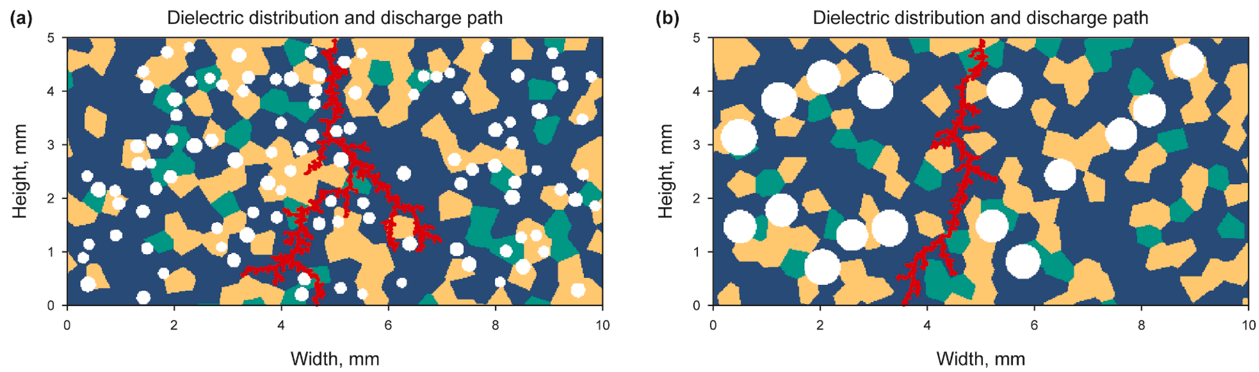

Fig. 11. Rocks with different pore diameters. (**a**) Rocks with pore diameters of 0.2–0.3 mm, (**b**) rocks with pore diameters of 0.6–0.7 mm.

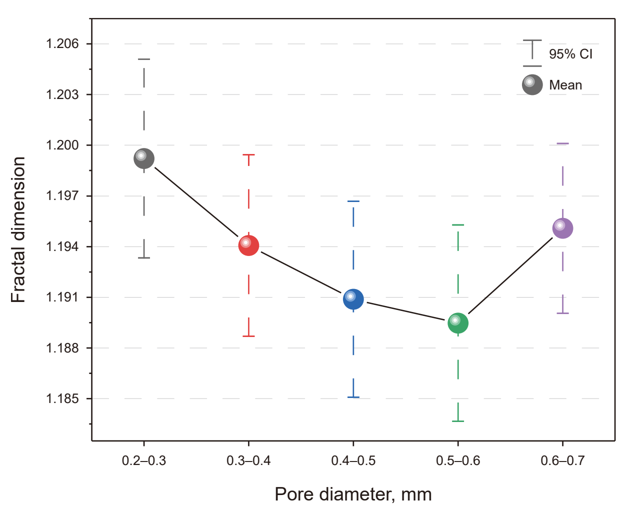

Fig. 12. Fractal dimension of breakdown path under different pore diameter conditions.

the particles in the breakdown path and the surrounding rock, which promotes thermal expansion of the heated particles. As the temperature increases, the rock particles expand and generate shock waves, resulting in the rapid initiation and propagation of fractures along the breakdown path.

When the loading time ranges from 1 to 10 μs, a complex network of cracks forms near the breakdown path, and a highly fragmented region, referred to as the crushed zone, develops. Additionally, radial cracks form inside the rock. The formation of the crushed zone is mainly associated with the continuous input of electrical energy and the rapid thermal expansion of particles along the breakdown path. The boundaries of the crushed zone extend under stresses generated by thermal expansion. The formation of radial cracks indicates the presence of tensile stress during stress transfer. Due to the low bonding strength between mineral crystals, the cracks propagate along inter-crystalline boundaries.

When the loading time ranges from 10 to 20 μs, only a limited number of new cracks develop within the rock, suggesting that most of the injected electrical energy has been dissipated. Additionally, the crushed zone formed along the breakdown path obstructs further transmission of energy into the rock interior.

Fig. 15 shows the evolution of the fracture field in porous rocks under HVEP. The damage processes of porous and non-porous rocks are generally similar, including fracture initiation, rapid fracture propagation, and energy dissipation stages. However, notable differences emerge in their damage characteristics. Specifically, radial cracks in porous rocks tend to connect to nearby pores during propagation. This behavior arises from local stress concentration zones that form around pores as compressive stress builds, making pore boundaries preferential paths for radial crack propagation.

To further assess the fragmentation effect, rock fragments from both porous and non-porous rocks were counted after loading, and their equivalent diameters were calculated using Eq. (12).

$$r_e = \sqrt{V_f / \pi} \tag{12}$$

where r_e is the equivalent radius of the fragment, mm; V_f is the area of the fragment, mm^2.

The cumulative distribution curve of equivalent fragment size is shown in Fig. 16. Based on the equivalent-diameter distribution, the post-fracture fragments can be classified into three size ranges: 0.016–0.8 mm (small fragments), 0.8–2.2 mm (medium fragments), and 2.2–2.63 mm (large fragments). Small fragments are mainly generated within the crushed zone, medium fragments are primarily formed in the radial crack zone, and large fragments are mainly associated with axial cleavage of the specimen.

Small and medium fragments are mainly produced by the direct crushing effect of HVEP. The volume fraction of small fragments is similar in porous and non-porous rocks, indicating that the crushed zone is only weakly influenced by the presence of pores. This is because the stress generated near the breakdown path significantly exceeds the rock strength, resulting in a similar crushing effect in this region.

However, the volume fraction of medium fragments is higher in porous rocks than in non-porous rocks. In addition, the medium fragments in porous rocks are mainly concentrated in the 1.0–1.14 mm range, which is larger than those in non-porous rocks.

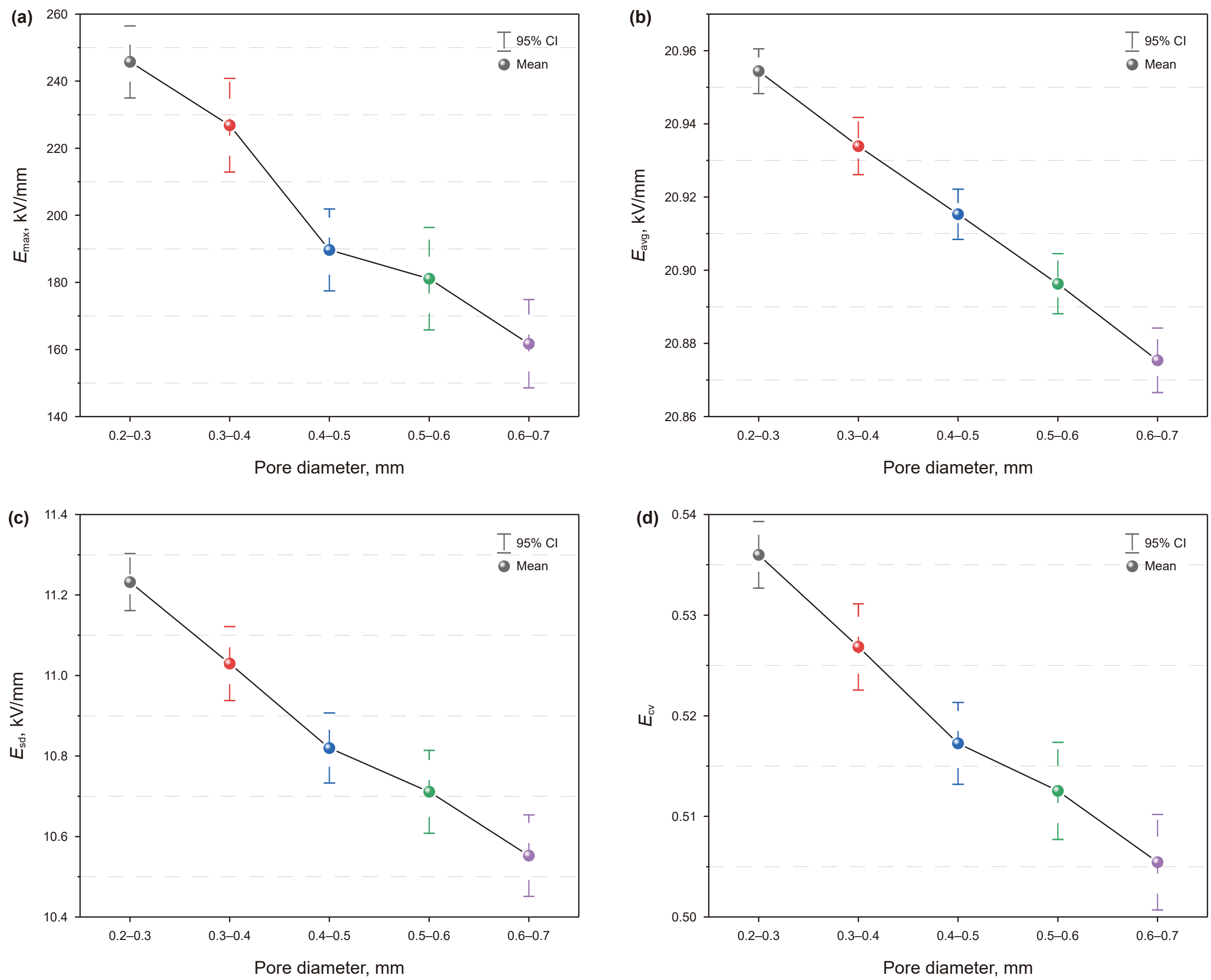

Fig. 13. Intensity of electric field in rock. (**a**) Maximum electric field intensity, (**b**) average electric field intensity, (**c**) standard deviation of electric field intensity, (**d**) coefficient of variation of electric field intensity.

This difference arises because stress concentration zones formed around pore boundaries promote crack initiation and propagation toward pores, thereby facilitating the interconnection of fractures and the formation of medium fragments.

3.3.2. Influence of pore diameter on rock fragmentation characteristics

Based on the findings in Section 3.3.1, rock fragmentation under HVEP exhibits three representative damage features: the crushed zone formed along the breakdown channel, the radial crack zone, and the macroscopic fragments generated by axial fracturing. The crushed zone and the radial crack zone result directly from electrical energy input and therefore reflect the crushing performance of HVEP rock breaking. On this basis, a quantitative evaluation system based on fragment-size distribution was established to assess the crushing effect and energy-utilization efficiency through statistical analysis of fragment volume and equivalent diameter in crushed zones and radial crack zones.

It should be noted that, unlike the absolute size-based classification adopted in Section 3.3.1 (small, medium, and large fragments), the evaluation system in this section uses a percentile-based classification for fragments in the crushed zone and radial crack zone. Specifically, all fragments in these two zones were classified into three groups: coarse fragments ($V > V_{75}$, 75th percentile), medium fragments ($V_{25} \le V \le V_{75}$), and fine fragments ($V < V_{25}$, 25th percentile).

$$S = 0.7S_c + 0.2S_f + 0.1S_u \tag{13}$$

where S is the total score, S_c, S_f, and S_u are the coarse-fragment score, fine-fragment score, and uniformity score, respectively. The coarse-fragment score was directly defined as its volume percentage:

$$S_c = V_c/V_{total} \times 100\% \tag{14}$$

where V_c is the total volume of coarse fragments, and V_{total} is the total volume of all analyzed fragments. A higher proportion of coarse fragments indicates lower energy consumption per unit volume of fragmented rock.

The fine-fragment score is calculated as follows:

$$S_f = 100\% - V_f\Big/V_{total} \times 100\% \tag{15}$$

where V_f is the total volume of fine fragments. This indicator reflects energy-utilization efficiency by penalizing excessive fine fragmentation.

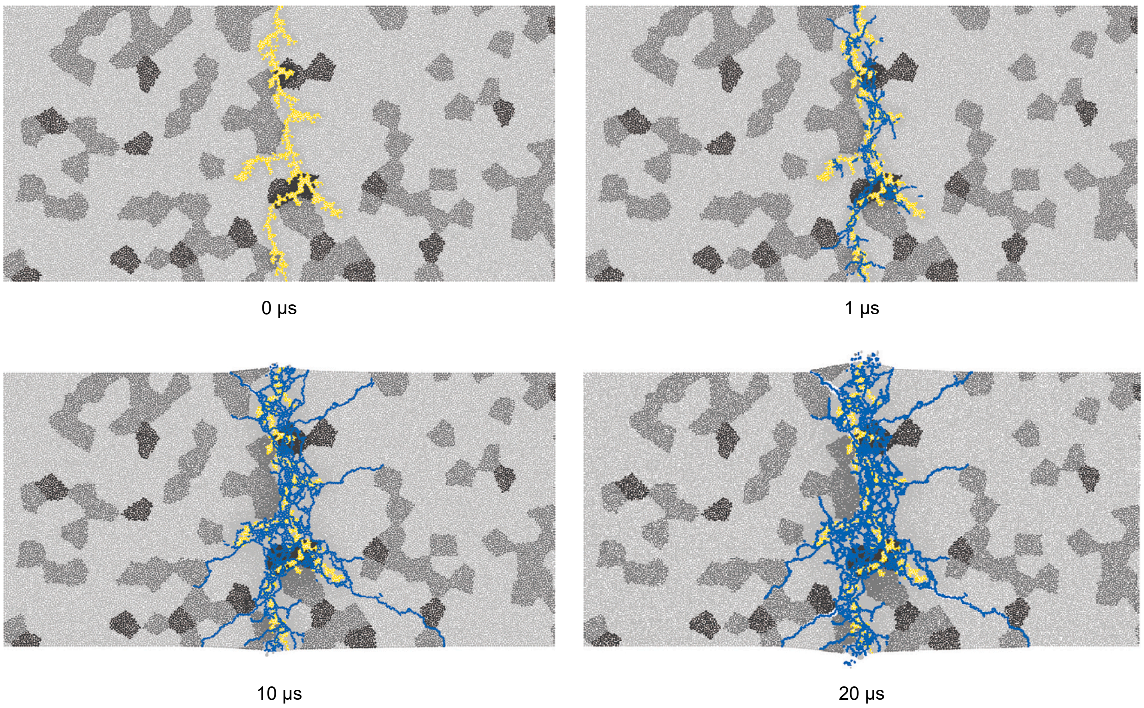

Fig. 14. Evolution of fracture field of non-porous rock under HVEP.

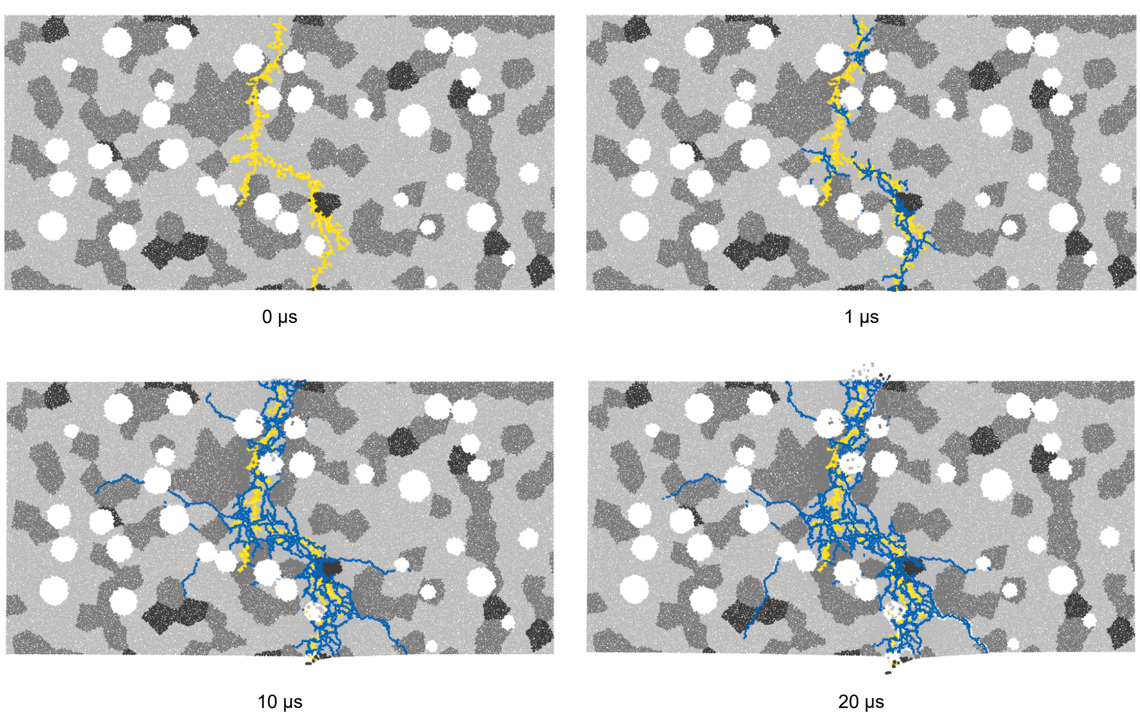

Fig. 15. Fracture field evolution of porous rock under HVEP.

The uniformity score is calculated based on the deviation of the actual fragment-size distribution from the target distribution (80% coarse fragments, 15% medium fragments, and 5% fine fragments by volume):

$$S_{\mathrm{u}} = 100\% - \sum \left|P_i - P_{t,i}\right| / 2 \tag{16}$$

where P_i is the volume percentage of fragments in class i in the actual distribution, $P_{t,i}$ is the corresponding ideal fraction in the target distribution, and i denotes the coarse-, medium-, and fine-fragment classes. This index reflects the uniformity and controllability of the particle size distribution of the fragments.

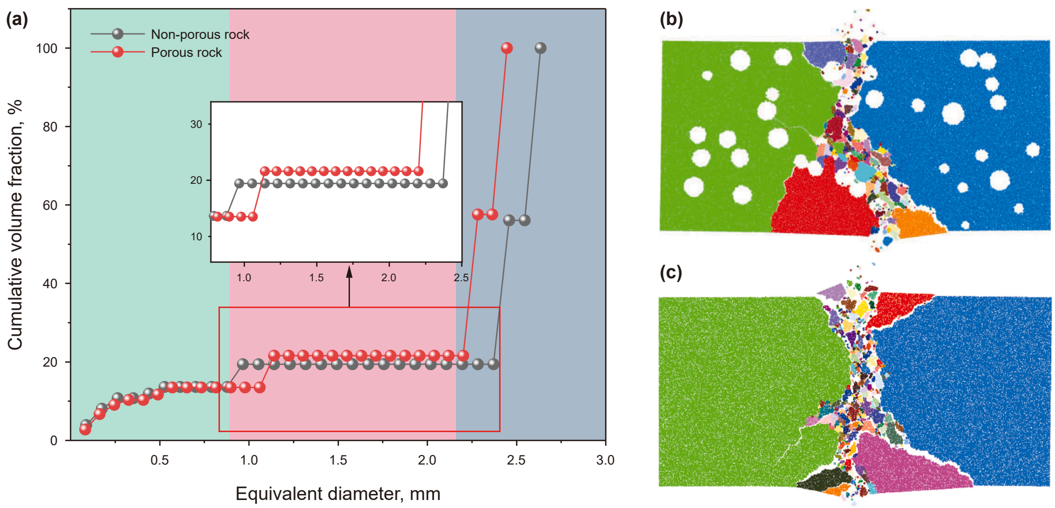

Fig. 16. Distribution of rock fragment sizes. (**a**) Cumulative volume-fraction curves for fragments with different equivalent diameters, (**b**) fragment-size distribution of porous rocks, (**c**) fragment-size distribution of non-porous rocks.

Fig. 17 shows that the rock-breaking performance under HVEP varies with pore diameter. The proportion of coarse fragments increases as pore diameter increases. Specifically, when the pore diameter is 0.2–0.3 mm, the average rock-breaking score is 29.50. When the pore diameter increases to 0.6–0.7 mm, the average score increases to 44.05. These results indicate that, under constant porosity, increasing pore diameter promotes the formation of coarse fragments under HVEP.

With constant porosity, smaller pore diameters result in a greater number of pores near the breakdown path. The shock wave generated along the breakdown path induces crack formation and interconnection between the pores, leading to the development of numerous cracks and small fragments along the path. These cracks and fragments cause the stress wave to gradually dissipate due to reflection and refraction during propagation. Therefore, for small pore diameters, the crushing characteristics are dominated by small fragments. As pore diameter increases, the number of pores decreases, and the proportion of coarse fragments formed by inter-pore crack linkage gradually increases.

However, as shown in Fig. 17(f), the increase in the crushing effect score gradually slows as the pore diameter increases. When the pore diameter reaches 0.6–0.7 mm, the crushing effect score becomes similar to that at 0.5–0.6 mm. This indicates that under constant porosity, larger pore sizes lead to better crushing effects. However, once the pore diameter exceeds a certain threshold, further improvement in the crushing effect becomes limited.

4. Mechanism analysis and engineering application

4.1. Mechanism analysis of electric pulse rock breaking in porous rocks

This study numerically investigates breakdown paths and rock damage characteristics for three rock conditions: porous rocks, non-porous rocks, and rocks with varying pore diameters. The results indicate that although the presence of pores reduces the complexity of HVEP breakdown paths, it substantially enhances the overall fragmentation efficiency of the rock. This finding

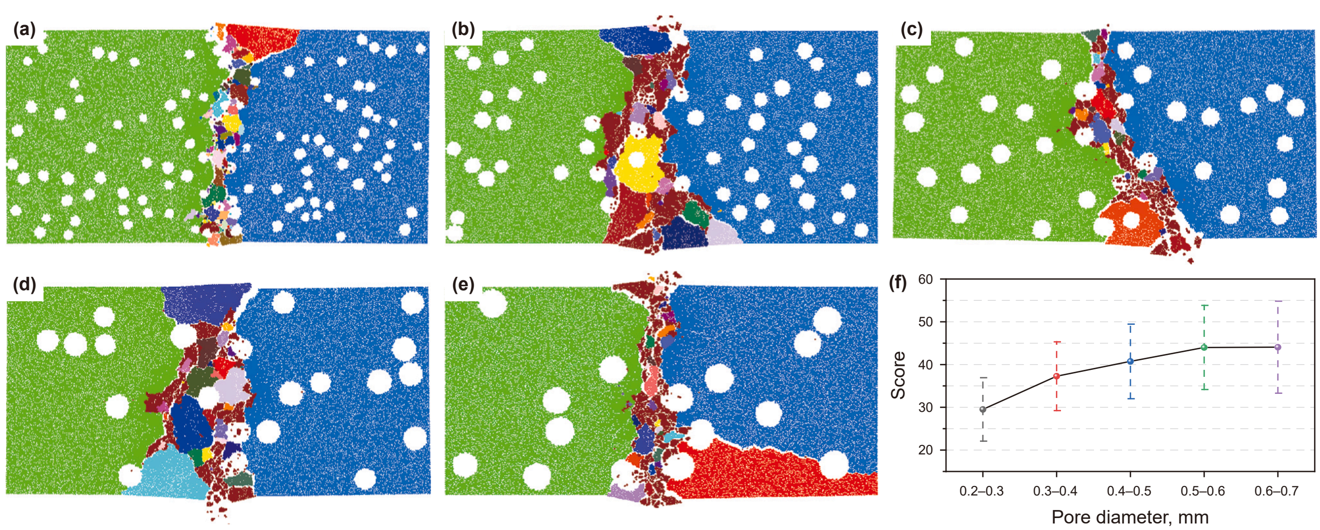

Fig. 17. Effect of rock damage by HVEP for rocks with different pore diameters. (**a**) 0.2–0.3 mm diameter, (**b**) 0.3–0.4 mm diameter, (**c**) 0.4–0.5 mm diameter, (**d**) 0.5–0.6 mm diameter, (**e**) 0.6–0.7 mm diameter, (**f**) scoring of the rock damage effect under the condition of different pore diameters.

suggests that, during HVEP-induced breakdown in porous rocks, the effects of pore structure on the breakdown path (i.e., the energy-injection channel) and on the rock mechanical response (i.e., energy absorption and damage) are distinct but interconnected. The following sections discuss the mechanisms by which pores influence breakdown paths, the stress concentration effects associated with pores, and the coupling between these two effects.

4.1.1. Control mechanism of pore structure on breakdown paths

In non-porous rocks, dielectric heterogeneity is primarily localized at mineral grain boundaries, resulting in a relatively uniform electric-field distribution. In the absence of pronounced electric-field gradients, multiple potential microscopic breakdown initiation sites compete randomly (Pietronero and Wiesmann, 1984). Consequently, breakdown-path propagation lacks a clear preferential direction and develops into a highly tortuous and branched morphology. Under these conditions, the geometry of the breakdown path is governed by the intrinsic mineralogical heterogeneity of the rock.

The introduction of pore structures fundamentally alters this dominant mechanism. The large contrast in relative permittivity between the gas within a pore and the surrounding rock matrix produces significant electric-field distortion and local field intensification at pore boundaries (Liu et al., 2023a). These localized high-field regions act as preferential breakdown channels that guide and constrain the breakdown propagation, thereby reducing its degrees of freedom. Finite-element studies have similarly shown that pore structures amplify field intensity and direct breakdown trajectories (Liu et al., 2023b). Thus, breakdown paths tend to propagate along these high-field zones, reducing tortuosity and branching. In this regime, pore geometry supersedes mineral heterogeneity as the primary determinant of breakdown-path trajectories. A schematic illustrating the pore-induced modulation of breakdown paths is provided in Fig. 18.

For a fixed porosity, the relationship between pore diameter and path complexity is nonlinear. Small pore diameters imply a larger number of pores, increasing the spatial discreteness of the electric-field distribution; this heightened spatial variability promotes branching and detours, yielding more complex paths. As the pore diameter increases, the number of pores decreases, and the field distribution becomes more homogeneous, leading to simpler breakdown paths. However, when the pore diameter exceeds a critical threshold (e.g., 0.6–0.7 mm in present models), the reduced pore count weakens the overall capacity of pores to regulate the electric field, and control reverts to mineral heterogeneity, causing path complexity to increase again. The influence of pore diameter on path complexity under constant porosity is illustrated in Fig. 19.

4.1.2. Mechanisms of pore structure on damage effects

More complex breakdown paths generally correspond to a wider spatial distribution of initial energy deposition. Nevertheless, our results show that porous rocks exhibit simplified breakdown paths while achieving enhanced fragmentation efficiency. These observations indicate that the final damage state of the rock depends not only on the spatial distribution of energy deposition, as reflected by the breakdown-path morphology, but also on the dynamic mechanical response of the rock.

The principal mechanism is stress concentration at pore interfaces. Kang et al. (2022) reported that the pressure waves generated during HVEP are analogous in waveform to blast-induced shock waves; consequently, the dynamic process induced by electrical breakdown may be regarded as explosion-like dynamic loading. Lan et al. (2024) showed that stress-wave reflection at free interfaces (i.e., pore boundaries) can induce substantial tensile stresses. Given that the tensile strength of rock is typically much lower than its compressive strength, pores become sites of high tensile stress. Fig. 20 presents contact force chains at 3 μs, delineating the internal force-transmission paths in the particulate medium, where blue and red denote compressive and tensile forces, respectively. Our numerical results are consistent with previous findings (Lan et al., 2024), showing that pronounced stress concentrations and tensile stresses occur near the breakdown paths and in regions adjacent to pores. Cracks therefore preferentially nucleate around pores and propagate by linking neighboring pores, eventually producing coarse fragments. Consequently, compared with non-porous rocks, porous rocks subjected to HVEP exhibit superior fragmentation performance.

We further consider the effect of pore diameter on fragmentation under constant porosity. Song et al. (2024) found that, under explosive loading, the spatial extent of stress-concentrated regions increases with pore diameter. Fig. 21 shows the force-chain patterns for rocks with pore diameters of 0.5–0.6 mm. Compared with smaller pores, larger pores induce broader tensile-stress zones, in agreement with the findings of Song et al. (2024). Moreover, Li et al. (2018a) demonstrated that pores may exert a crack-arresting effect governed by inter-pore spacing, whereby reduced pore spacing enhances crack arrest. Li et al. (2021) further suggested that, compared with pore diameter, pore spacing exerts a more pronounced influence on rock fragmentation. Our simulations indicate that, at fixed porosity, increasing pore diameter increases the proportion of large fragments after failure. This outcome arises from two competing effects. On the one hand, larger pores expand the regions of stress concentration. On the other hand, smaller pore diameters produce a more densely distributed pore network, which enhances the crack-arresting effect. As pore diameter increases, inter-pore spacing also increases,

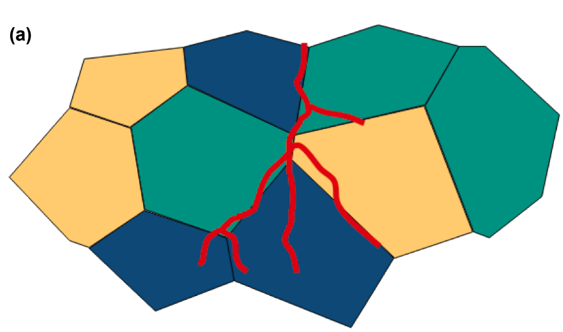

Fig. 18. Effect of pores on breakdown path.

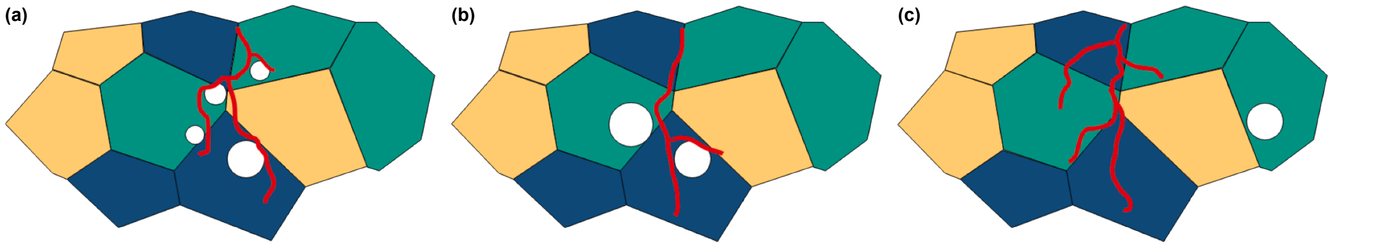

Fig. 19. Effect of pore diameter on breakdown path.

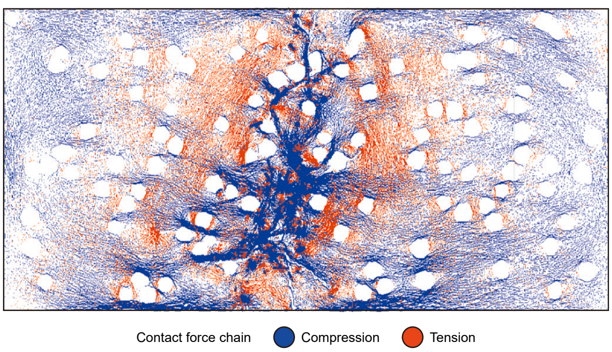

Fig. 20. Internal force chain diagram for rocks with 0.2–0.3 mm pores.

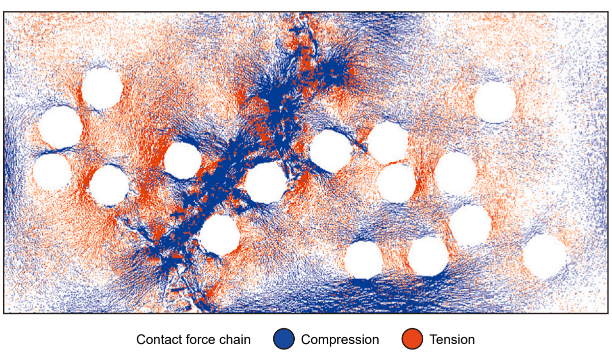

Fig. 21. Internal force chain diagram for rocks with 0.6–0.7 mm pores.

and the crack-arresting effect weakens, thereby facilitating crack coalescence between pores and the formation of larger fragments. However, when pore diameter increases further and the number of pores declines substantially, the increasing inter-pore spacing inhibits crack propagation and coalescence between pores, thereby limiting the formation of very large fragments. Accordingly, the improvement in fragmentation effectiveness with increasing pore diameter exhibits a diminishing trend.

4.1.3. Analysis of the effect of breakdown path and pore coupling on rock damage

In summary, breakdown-path complexity determines the initial spatial distribution of energy deposition, whereas the pore structure governs the resulting dynamic stress state and energy-dissipation modes that drive fragmentation. The interaction between these two mechanisms yields distinct damage outcomes. Our simulations show that rocks with many small pores produce more complex breakdown paths than rocks with large pores, yet their fragmentation efficiency is lower than that of rocks with large pores. This observation indicates that pore-induced modifications to the dynamic stress field dominate the fragmentation outcome and may exert a greater influence than the morphology of the breakdown path itself.

4.2. Recommendations for engineering applications

HVEP rock-breaking technology, characterized by controllable energy input and low energy consumption, offers an effective solution for deep rock fragmentation. This study analyzes the influence of pore structure on rock fragmentation under HVEP and provides practical recommendations for field applications.

In tunnel excavation and mining, the fragmentation behavior of porous rocks under HVEP can be exploited to improve drilling efficiency. Numerical results indicate that pores promote the formation of large fragments while reducing the generation of fine particles. In contrast, conventional methods such as drilling and blasting or mechanical cutting offer limited control over fragment size and often generate excessive dust. HVEP allows discharge parameters to be optimized according to porosity and pore-size distribution, thereby improving energy utilization and reducing dust pollution.

Pore diameter and inter-pore spacing play crucial roles in fragmentation efficiency. Larger pores facilitate crack initiation, whereas excessively dense pore distributions may hinder crack propagation. Engineering designs can therefore introduce or modify pore structures to enhance rock-breaking performance, particularly in hard-rock tunneling. Compared with laser-based thermal rock breaking, which relies on melting and consumes more energy, HVEP achieves higher efficiency and better controllability.

In fractured or porous formations, HVEP can guide breakdown paths to form interconnected fracture networks, thereby enhancing resource recovery in geothermal or shale gas extraction. It can also be applied for targeted weakening in high-stress zones to alleviate stress concentration and improve rock-mass stability. Overall, HVEP demonstrates strong adaptability and controllability in deep resource extraction under complex geological conditions.

4.3. Limitations and outlook

In this study, certain simplifications were made in the model construction to focus on the intrinsic influence of pore geometry on electrical breakdown and rock fragmentation under HVEP. The current numerical model does not consider the electrical properties of pore fluids or their effects on the mechanical response of the rock. In fact, the dielectric characteristics of pore fluids can alter the electric-field distribution and breakdown path and may further influence stress-wave propagation and energy dissipation, thereby changing the fracture pattern of the rock. Therefore, the present simulation results primarily reflect the role of pore geometry under idealized conditions.

Future studies will aim to develop a more comprehensive electro-thermal-fluid-mechanical coupling model. By incorporating fluid-flow governing equations into the discrete-element framework, the proposed model will systematically investigate how pore fluids with different dielectric properties (e.g., water and drilling fluids) influence the HVEP-induced rock fragmentation mechanism. Such research is expected to elucidate the key physical processes underlying fluid-electric-mechanical coupling and provide theoretical guidance for the development of efficient rock-breaking technologies under complex geological conditions.

5. Conclusions

This study developed a numerical framework that integrates the FDM, a stochastic propagation model, and a thermo-mechanical DEM to elucidate the governing effects of pore structure on rock-breaking mechanisms under HVEP. The major findings are summarized as follows.

(1) Pore structures significantly modulate breakdown-path complexity. In dense rocks, path propagation is predominantly influenced by mineral heterogeneity, yielding highly branched patterns. In contrast, in porous rocks, electric-field enhancement at pore boundaries guides path propagation and reduces branching complexity.
(2) Under constant porosity, breakdown-path complexity exhibits a nonlinear decrease–increase trend with increasing pore diameter. This behavior results from the competitive transition between pore-dominated and heterogeneity-dominated propagation mechanisms.
(3) Pores act as free interfaces that induce localized stress concentrations during plasma channel expansion, making pore boundaries preferential crack-initiation sites. This mechanism significantly promotes crack initiation and propagation, thereby improving fragmentation efficiency.
(4) The modification of the stress field induced by pores exerts a greater influence on fragmentation efficiency than the breakdown-path morphology itself. Although smaller pores generate more complex breakdown paths, larger pores (e.g., 0.6–0.7 mm) lead to wider stress concentration zones and enhance fragmentation. However, when the pore diameter increases from 0.5–0.6 mm to 0.6–0.7 mm, the improvement becomes marginal, indicating that further increasing the pore diameter beyond approximately 0.6 mm provides only limited additional improvement under the conditions of this study.

These results advance the theoretical understanding of HVEP rock breaking in porous media and provide a practical basis for optimizing discharge parameters according to pore characteristics to improve rock-breaking efficiency and energy utilization. Nevertheless, the present model does not incorporate the electrical and dynamic effects of pore fluids, which may affect the accuracy of electric-field and stress-wave predictions. Future work will focus on developing a fully coupled electro–thermal–hydro–mechanical (E–T–H–M) model to investigate the role of pore fluids with different dielectric properties, thereby further enhancing the engineering applicability and robustness of the proposed framework.

CRediT authorship contribution statement

Yu-Wei Li: Writing – review & editing, Methodology, Funding acquisition. **Xin-Hui Guo:** Writing – original draft, Software, Conceptualization. **Xue-Wei Liu:** Visualization, Software. **Yuan Pan:** Visualization, Software. **Yong-Hui Xiao:** Formal analysis. **Hui-Min Tang:** Investigation. **Dmitriy A. Martyushev:** Investigation. **Zi-Han Sun:** Project administration, Investigation, Data curation.

Availability of data and materials

The data and materials used to support the findings of this study are included within the article.

Declaration of competing interest

The authors declare that they have no conflict of interest.

Acknowledgements

This work was supported by the Doctoral Start-up Foundation of Liaoning Province (No. 2025-BS-0291), the Young Scientists Fund of the National Natural Science Foundation of China (No. 52404217), and the National Natural Science Foundation of China (NSFC) Major Research Instrument Development Project (No. 52427805).

References

Abdelaziz, A., Zhao, Q., Grasselli, G., 2018. Grain based modelling of rocks using the combined finite-discrete element method. Comput. Geotech. 103, 73–81. https://doi.org/10.1016/j.compgeo.2018.07.003.
Ahrens, T.J., 1995. Mineral Physics & Crystallography: A Handbook of Physical Constants. American Geophysical Union, Washington, DC.
Biela, J., Marxgut, C., Bortis, D., et al., 2009. Solid state modulator for plasma channel drilling. IEEE Trans. Dielectr. Electr. Insul. 16 (4), 1093–1099. https://doi.org/10.1109/TDEI.2009.5211860.
Bloch, S., Lander, R.H., Bonnell, L., 2002. Anomalously high porosity and permeability in deeply buried sandstone reservoirs: origin and predictability. AAPG Bull. 86 (2), 301–328. https://doi.org/10.1306/61EEDABC-173E-11D7-8645000102C1865D.
Burkin, V.V., Kuznetsova, N.S., Lopatin, V.V., 2009. Dynamics of electro burst in solids: I. Power characteristics of electro burst. J. Phys. D Appl. Phys. 42 (18), 185204. https://doi.org/10.1088/0022-3727/42/18/185204.
Cong, Z.Y., Liu, J., Ranjith, P.G., et al., 2026. Numerical investigation of the influence of fracture morphology on enhanced geothermal system (EGS) development using the discrete element method. Energy Convers. Manag. 348, 120669. https://doi.org/10.1016/j.enconman.2025.120669.
Feng, W.K., Rao, P.P., Cui, J.F., et al., 2024. Multiphysics multicoupled modeling of rock fragmentation under high-voltage electrical pulse. Int. J. GeoMech. 24 (9), 04024176. https://doi.org/10.1061/IJGNAI.GMENG-9298.
Fu, J., Zeng, G.Y., Zhang, H., et al., 2022. Experimental investigation on wear behaviors of TBM disc cutter ring with different cooling methods. Eng. Fail. Anal. 134, 106076. https://doi.org/10.1016/j.engfailanal.2022.106076.
Fu, Y.K., Wu, Y.Z., Li, J.C., et al., 2024. Mechanical properties and energy evolutions of burst-prone coal samples with holes and fillings. Int. J. Coal Sci. Technol. 11 (1). https://doi.org/10.1007/s40789-024-00675-z.
Gulbin, Y.L., Evangulova, E.B., 2003. Morphometry of quartz aggregates in granites: fractal images referring to nucleation and growth processes. Math. Geol. 35 (7), 819–833. https://doi.org/10.1023/B:MATG.0000007781.90498.5e.
Hassanpour, J., 2018. Development of an empirical model to estimate disc cutter wear for sedimentary and low to medium grade metamorphic rocks. Tunn. Undergr. Space Technol. 75, 90–99. https://doi.org/10.1016/j.tust.2018.02.009.
Huang, W., Shi, F.N., 2019. Selective breakage of mineralised synthetic particles by high voltage pulses. Part 1: metalliferous grain-induced breakage in a two-particle paired system. Miner. Eng. 134, 261–268. https://doi.org/10.1016/j.mineng.2019.02.024.
Ji, S.T., Karlovšek, J., 2022. Calibration and uniqueness analysis of microparameters for DEM cohesive granular material. Int. J. Min. Sci. Technol. 32 (1), 121–136. https://doi.org/10.1016/j.ijmst.2021.11.003.
Jin, X., Rao, P.P., Feng, W.K., et al., 2026. Modelling of rock fragmentation under combined actions of high voltage electropulse and mechanical drilling. Geoenergy Sci. Eng. 256, 214128. https://doi.org/10.1016/j.geoen.2025.214128.
Joll, K., Schienbein, P., Rosso, K.M., et al., 2024. Machine learning the electric field response of condensed phase systems using perturbed neural network potentials. Nat. Commun. 15 (1), 8192. https://doi.org/10.1038/s41467-024-52491-3.
Kang, J.F., Li, C.P., Duan, L.C., et al., 2022. An experimental and numerical study on the mechanism of high-voltage electro pulse rock-breaking. Rock Mech. Rock Eng. 56 (3), 2185–2195. https://doi.org/10.1007/s00603-022-03154-6.
Lan, R.Y., Cheng, R.S., Zhou, Z.L., et al., 2024. Damage and fragmentation of rock under multi-long-hole blasting with large empty holes. Rock Mech. Rock Eng. 57 (9), 7603–7622. https://doi.org/10.1007/s00603-024-03942-2.

Li, M., Zhu, Z.M., Liu, R.F., et al., 2018a. Study of the effect of empty holes on propagating cracks under blasting loads. Int. J. Rock Mech. Min. Sci. 103, 186–194. https://doi.org/10.1016/j.ijrmms.2018.01.043.
Li, X.B., Li, C.J., Cao, W.Z., et al., 2018b. Dynamic stress concentration and energy evolution of deep-buried tunnels under blasting loads. Int. J. Rock Mech. Min. Sci. 104, 131–146. https://doi.org/10.1016/j.ijrmms.2018.02.018.
Li, X.L., Li, Q., Wang, J.G., et al., 2021. Influence of hole arrangement on the section of cavity formed by cutting blast. Geofluids 2021 (1), 1–12. https://doi.org/10.1155/2021/9080560.
Li, Y., Yang, R.S., Wang, Y.B., et al., 2024. Influence of water coupling coefficient on the blasting effect of red sandstone specimens. Int. J. Coal Sci. Technol. 11 (1), 8. https://doi.org/10.1007/s40789-023-00620-6.
Lin, Y.X., Li, C.H., Ma, J.J., et al., 2022. Effects of void morphology on fracturing characteristics of porous rock through a finite-discrete element method. J. Nat. Gas Sci. Eng. 104, 104684. https://doi.org/10.1016/j.jngse.2022.104684.
Lisitsyn, I.V., Inoue, H., Katsuki, S., et al., 1999. Drilling and demolition of rocks by pulsed power. In: Digest of Technical Papers. 12th IEEE International Pulsed Power Conference, pp. 169–172. https://doi.org/10.1109/PPC.1999.825439.
Liu, W.J., Zhang, J.H., Tang, W.J., et al., 2025. Mechanism of rock breaking by high voltage electric pulse liquid plasma shockwave breaking. J. Appl. Geophys. 243, 105962. https://doi.org/10.1016/j.jappgeo.2025.105962.
Liu, W.J., Zhang, Y.J., Zhu, X.H., et al., 2023a. Influence of pore characteristics inside formation on partial electrical breakdown in electric impulse drilling. IEEE Trans. Plasma Sci. 51 (6), 1413–1426. https://doi.org/10.1109/TPS.2023.3273544.
Liu, W.J., Zhang, Y.J., Zhu, X.H., et al., 2023b. The influence of pore characteristics on rock fragmentation mechanism by high-voltage electric pulse. Plasma Sci. Technol. 25 (5), 055502. https://doi.org/10.1088/2058-6272/acab42.
Liu, W.J., Zhang, Y.J., Zhu, X.H., 2023c. The partial electrical breakdown mechanism by high voltage electric pulses in multi-fractured granite. Geomech. Energy Environ. 34, 100459. https://doi.org/10.1016/j.gete.2023.100459.
Liu, X.H., Liu, S.Y., Ji, H.F., 2015. Numerical research on rock breaking performance of water jet based on SPH. Powder Technol. 286, 181–192. https://doi.org/10.1016/j.powtec.2015.07.044.
Liu, X.N., Duan, L.C., Li, C.P., et al., 2024. Simulation and experimental study on the rock-breaking process induced by high-voltage electric pulse. Rock Mech. Rock Eng. 57 (8), 6141–6161. https://doi.org/10.1007/s00603-024-03843-4.
Nagel, J.R., 2011. Solving the Generalized Poisson Equation Using the finite-difference Method (FDM). Lecture Notes, Dept. of Electrical and Computer Engineering, vol. 52. University of Utah.
Nagel, J.R., 2014. Numerical solutions to poisson equations using the finite-difference method. IEEE Antenn. Propag. Mag. 56 (4), 209–224. https://doi.org/10.1109/MAP.2014.6931698.
Noskov, M.D., Kukhta, V.R., Lopatin, V.V., 1995. Simulation of the electrical discharge development in inhomogeneous insulators. J. Phys. D Appl. Phys. 28 (6), 1187–1194. https://doi.org/10.1088/0022-3727/28/6/024.
Pietronero, L., Wiesmann, H.J., 1984. Stochastic model for dielectric breakdown. J. Stat. Phys. 36 (5), 909–916. https://doi.org/10.1007/BF01012949.
Potyondy, D.O., Cundall, P.A., 2004. A bonded-particle model for rock. Int. J. Rock Mech. Min. Sci. 41 (8), 1329–1364. https://doi.org/10.1016/j.ijrmms.2004.09.011.
Qiao, W., Li, W.P., Zhang, X., 2013. Characteristic of water chemistry and hydrodynamics of deep karst and its influence on deep coal mining. Arab. J. Geosci. 7 (4), 1261–1275. https://doi.org/10.1007/s12517-013-0899-0.
Quan, J.S., Rong, G., Xu, L.D., et al., 2023. A three-dimensional grain-based model for studying the microscopic fracture behaviour of granite. Comput. Geotech. 159, 105427. https://doi.org/10.1016/j.compgeo.2023.105427.
Schiegg, H.O., Rødland, A., Zhu, G.Z., et al., 2015. Electro-pulse-boring (EPB): novel super-deep drilling technology for low cost electricity. J. Earth Sci. 26 (1), 37–46. https://doi.org/10.1007/s12583-015-0519-x.
Song, S.S., Huo, R.K., Liang, Y.L., et al., 2024. Numerical simulation and application research of straight-hole cut blasting with empty holes in railway tunnels. Int. J. GeoMech. 24 (4), 04024037. https://doi.org/10.1061/IJGNAI.GMENG-9183.
Sun, H.K., Gan, D.Q., Liu, Z.Y., et al., 2025. Fracture mechanism and dynamic compressive strength prediction of microwave-assisted stress wave magnetite blasting based on GA-LSTM. Bull. Eng. Geol. Environ. 85 (1). https://doi.org/10.1007/s10064-025-04711-3.
Surma, F., Geraud, Y., 2003. Porosity and thermal conductivity of the soultz-sous-forêts granite. Pure Appl. Geophys. 160 (5–6), 1125–1136. https://doi.org/10.1007/PL00012564.
Vogler, D., Walsh, S.D.C., Saar, M.O., 2020. A numerical investigation into key factors controlling hard rock excavation via electropulse stimulation. J. Rock Mech. Geotech. Eng. 12 (4), 793–801. https://doi.org/10.1016/j.jrmge.2020.02.002.
Wang, W., Pan, Y.S., Zhao, H.R., et al., 2026. Electric charge induction monitoring of deformation and failure behavior of igneous rock: laboratory test and field application. J. Rock Mech. Geotech. Eng. 18 (2), 861–886. https://doi.org/10.1016/j.jrmge.2025.03.032.
Wei, J.P., Wang, M.Y., Liu, Y., et al., 2026. Study on the fracture characteristics of pre-grooved rock under particle impact. Eng. Fract. Mech. 337, 112006. https://doi.org/10.1016/j.engfracmech.2026.112006.
Xie, H.P., Lu, J., Li, C.B., et al., 2022. Experimental study on the mechanical and failure behaviors of deep rock subjected to true triaxial stress: a review. Int. J. Min. Sci. Technol. 32 (5), 915–950. https://doi.org/10.1016/j.ijmst.2022.05.006.
Yang, L., Gao, M.Z., Yang, B.G., et al., 2025. Mechanisms of drillability enhancement and damage evolution in granite under coupled laser-drill interaction. Rock Mech. Rock Eng. 59, 5341–5363. https://doi.org/10.1007/s00603-025-04963-1.
Yang, S.Q., Tian, W.L., Huang, Y.-H., 2018. Failure mechanical behavior of pre-holed granite specimens after elevated temperature treatment by particle flow code. Geothermics 72, 124–137. https://doi.org/10.1016/j.geothermics.2017.10.018.
Zhang, Q.Y., Wang, G.L., Pan, X.D., et al., 2023a. High voltage electric pulse drilling: a study of variables through simulation and experimental tests. Energies 16 (3), 1174. https://doi.org/10.3390/en16031174.
Zhang, T., Yu, L.Y., Ju, M.H., et al., 2023b. Effect of grain size on the dynamic flexural tensile strength of granite: insight from GBM3D-PFC simulations. Int. J. Geo-Mech. 23 (5), 04023046. https://doi.org/10.1061/IJGNAI.GMENG-7756.
Zhang, T., Yu, L.Y., Peng, Y.X., et al., 2022. Influence of grain size and basic element size on rock mechanical characteristics: insights from grain-based numerical analysis. Bull. Eng. Geol. Environ. 81 (9), 347. https://doi.org/10.1007/s10064-022-02856-z.
Zhang, Z., Pei, Y., Liu, Z., et al., 2012. Experimental research on rock breakdown under short high-voltage pulse. High Volt. Eng. 38 (7), 1719–1725 (in Chinese).
Zhao, Y., Liu, Y., Cheng, J., et al., 2024. Prediction of plasma path and analysis of axial fracturing properties in rock fragmentation by high-voltage pulsed discharge (RHPD). J. Phys. D Appl. Phys. 57 (32), 325502. https://doi.org/10.1088/1361-6463/ad44a1.
Zhao, Y., Liu, Y., Liao, H.B., et al., 2025. Influence of electrode size on the fragmentation process of rocks with different heterogeneities under high-voltage pulses. Rock Mech. Rock Eng. 58 (3), 3653–3682. https://doi.org/10.1007/s00603-024-04340-4.
Zheng, Y., He, L., 2021. TBM tunneling in extremely hard and abrasive rocks: problems, solutions and assisting methods. J. Cent. South Univ. 28 (2), 454–480. https://doi.org/10.1007/s11771-021-4615-z.
Zhou, Z.L., Tan, Z.S., Li, Z.L., et al., 2021. TBM cutter wear under high-strength surrounding rock conditions: a case study from the second phase of the northern Xinjiang water supply project. Rock Mech. Rock Eng. 54 (9), 5023–5039. https://doi.org/10.1007/s00603-021-02545-5.
Zhu, X.H., Liu, S.Q., Liu, W.J., et al., 2024. Growth mechanism of three-dimensional plasma channels in high-voltage electric pulse rock breaking. Rock Mech. Rock Eng. 57 (11), 9477–9496. https://doi.org/10.1007/s00603-024-03969-5.
Zhu, X.H., Luo, Y.X., Liu, W.J., 2020. On the rock-breaking mechanism of plasma channel drilling technology. J. Pet. Sci. Eng. 194, 107356. https://doi.org/10.1016/j.petrol.2020.107356.
Zhu, X.H., Luo, Y.X., Liu, W.J., et al., 2021. On the mechanism of high-voltage pulsed fragmentation from electrical breakdown process. Rock Mech. Rock Eng. 54 (9), 4593–4616. https://doi.org/10.1007/s00603-021-02537-5.